Taylor & Francis
Taylor & Francis Group

RESEARCH ARTICLE

Multimodal imaging and photothermal synergistic immunotherapy of retinoblastoma with tuftsin-loaded carbonized MOF nanoparticles

Hongmi Zou[a*], Meng Li[a*], Xing Li[a*], Wendi Zheng[a], Hongyu Kuang[b], Menglei Wang[a], Wenli Zhang[c], Haitao Ran[d], Huafeng Ma[a] and Xiyuan Zhou[a]

[a]Department of Ophthalmology, The Second Affiliated Hospital of Chongqing Medical University, Chongqing, PR China; [b]Department of Cardiology, The Second Affiliated Hospital of Chongqing Medical University, Chongqing, PR China; [c]Department of Radiology, The Second Affiliated Hospital of Chongqing Medical University, Chongqing, PR China; [d]Department of Ultrasound, Chongqing Key Laboratory of Ultrasound Molecular Imaging, The Second Affiliated Hospital of Chongqing Medical University, Chongqing, PR China

ABSTRACT

Retinoblastoma (Rb) represents 3% of all childhood malignancies and seriously endangers children's lives and quality of life. Early diagnosis and treatment can save children's vision as much as possible. Multifunctional nanoparticles have become a research hotspot in recent years and are expected to realize the integration of early diagnosis and early treatment. Therefore, we report a nanoparticle with dual-mode imaging, photothermal therapy, and immune activation: carbonized MOF nanoparticles (CM NPs) loaded with the immune polypeptide tuftsin (CMT NPs). The dual-mode imaging ability, antitumor effect, and macrophage immunity activation ability of these nanoparticles combined with laser irradiation were studied. The biosafety of CMT NPs was detected. The multifunctional magnetic nanoparticles enhanced photoacoustic (PA) and magnetic resonance (MR) imaging in vivo and in vitro, facilitating diagnosis and efficacy evaluation. The combined effect of CMT NPs and laser irradiation was recorded and verified. Through the accumulation of magnetic field nanoparticles in tumors, the photothermal conversion of nanoparticles under laser irradiation led directly to tumor apoptosis/necrosis, and the release of tuftsin induced macrophage M1-type activation, resulting in antitumor immune effects. Enhanced PA/MR imaging CMT NPs have great potential in dual-mode image-guided laser/immune cotherapy. The nanoparticles have high biosafety and have potential in cancer treatment.

1. Introduction

Retinoblastoma (Rb), with a worldwide incidence of 1:15,000 to 1:20,000 live births, is the most common primary intraocular malignancy in childhood. Although Rb is rare, it has become a cornerstone of cancer management protocols in oncology, including classification protocols, treatment modalities, genetic testing and screening. Rb is the only type of childhood cancer that does not require a pathologically confirmed diagnosis because of the vital role of assistive tests, such as ophthalmic assistive imaging, ultrasound, and MRI, in the differential diagnosis and staging of opaque eyes. These imaging modalities have become key to the subclinical detection and monitoring of both tumor and nontumor events during conservative treatment, with profound implications for both treatment strategies and eventual clinical outcomes. Thus, the improvement of image diagnostic efficiency of Rb is helpful to promote the overall management of the disease (Munier et al., 2020). Until slightly more than half a century ago, Rb had a poor prognosis and was fatal in most children, with the main treatment being removal of the eyeball. In a short period of time, the cancer management of Rb has advanced immensely, along with the development of specialized centers, better infrastructure and improved disease awareness, resulting in near-100% survival rates for children in developed countries, even saving the eye in many cases (Fabian et al., 2018). Although Rb is now the most curable childhood cancer and has a high survival rate, advanced tumors limit overall rescue, and the advent of chemotherapy has improved treatment outcomes. However, more effective and less toxic molecular targeted therapy is still an urgent problem to be solved (Kaewkhaw & Rojanaporn, 2020).

Nanomedicine is a type of submicron drug delivery system designed to improve drug delivery to tumors while reducing systemic side effects, which has been widely studied in the oncology field in recent years (de Maar et al., 2020). There are several principles for targeting oncology drugs: passive targeting (relying mainly on enhanced permeability and retention (EPR) effects) (Nichols & Bae, 2014; Wang et al., 2018), active targeting (using vectors modified with tumor-specific targeting antibodies, magnetic targeting)

(Wu et al., 2018; Guo et al., 2019), or triggered release (nano-carrier release drugs under thermal, ultrasonic, or light effects) (Arranja et al., 2017; Wang et al., 2020). Previously, folic acid-targeted liposome nanoparticles and magnetic targeted gold nanocages have been applied to the imaging and treatment of Rb with initial success (Wu et al., 2018; Wang et al., 2020). However, considering the poor stability of liposome nanoparticles and the high cost of gold nanocages, the exploration of new nanomaterials has become a research direction.

In recent years, MOFs, especially nanoscale MOFs, have received much attention in the development of drug delivery and tumor therapy platforms (Wu & Yang, 2017). Compared with traditional drug carriers, MOFs have different morphology, composition, size, and chemical properties, enabling a variety of functions and stimulus-responsive controlled drug release (Bowser et al., 2018). The enlarged specific surface area and high porosity of MOFs increase their carrying capacity (Karami et al., 2021). Moreover, the weak coordination bond ensures the biodegradability of MOFs (Singh et al., 2021). MOFs are an ideal base material for carbonization due to their high carbon content, uniform composition, and regular structure (Liang et al., 2018; Li et al., 2019). Porous carbon prepared by the carbonization method has the characteristics of a large specific surface area, high porosity, and good chemical stability. In summary, MOFs and their carbonized derivatives are promising platforms for drug delivery, clinical oncology, and other diseases.

Nanoparticle-based photothermal therapy (PTT) is a novel cancer treatment method that uses photothermal nanomaterials to convert light energy into heat to kill cancer cells. Direct thermal ablation (more than 42 °C) has an antitumor effect, killing tumor cells by destroying the tumor cell membrane, destroying the cytoskeleton and inhibiting DNA synthesis. It is suitable for solid tumors (Hou et al., 2018). Over the past decade or so, advances in cancer immunology have forced scientists and clinicians to acknowledge the extent to which suppressing cancer cells alone is not enough to effectively treat cancer. Tumors and their microenvironment are complex aggregates of transformed cells, blood vessels, fibroblasts, and immune cells that produce cytokines, which enhance the growth of tumor cells and inhibit the activation of antitumor immunity. Immunotherapy is a treatment that works on the immune system by activating the immune system to alter the tumor microenvironment, thereby killing rapidly dividing tumor cells (Musetti & Huang, 2018). The work of Guo and Li et al. confirmed the effectiveness of photothermal combined immunotherapy for tumor suppression (Guo et al., 2019; Li et al., 2019).

Studies have shown that TAMs participate in the immunosuppression, invasion and metastasis of tumors. Macrophages can be roughly divided into M1 macrophages and M2 macrophages according to their functions. M1 macrophages are involved in the inflammatory response, pathogen clearance, and antitumor immunity. In contrast, M2 macrophages affect the anti-inflammatory response and wound healing and have protumor properties (Mantovani et al., 2007; Komohara et al., 2016). Guerra et al. found that

hydrogels embedded in M1 macrophages upregulated nitrite and tumor necrosis factor α (TNF-α) to activate caspase-3 to induce tumor apoptosis, resulting in apoptosis of HCC cells *in vivo* and *in vitro* (Guerra et al., 2017). Piña et al. found that Rb tumor load increased after M1 TAMs were reduced (Piña et al., 2010). The study of Yamamoto N's team suggested that macrophages activated by PTII have a killing effect on Rb tumors, and the activation of macrophages is the first step of immune enhancement (Yamamoto et al., 1994). Therefore, M1-type macrophage induction may be an effective immunotherapy approach for Rb. Tuftsin is a tetrapeptide with the structure of Thr-Lys-Pro-Arg. Its activity is mainly related to the function of the immune system, especially macrophages, which can activate macrophages and induce M1-type polarization (Fridkin & Najjar, 1989). However, tuftsin has a short half-life *in vivo* and is easily hydrolyzed, which limits its application and development (An et al., 2014). The encapsulation of MOF nanoparticles can prevent rapid hydrolysis of the drug *in vivo*, thus improving its efficacy.

The purpose of this study was to construct carbonized MOF nanoparticles (CM NPs) coated with tuftsin (CMT NPs), which not only supports photoacoustic (PA)/magnetic resonance (MR) dual-mode imaging but also has a good photothermal/immunotherapeutic effect. CMT nanoparticles have high biosafety, and the magnetism obtained after carbonization enables them to transfer tuftsin to the target tissue (Huo et al., 2017), thus improving the photothermal/immunotherapy effect of tumors and effectively inhibiting tumors. By enhancing PA/MR imaging and inhibiting tumor growth, multifunctional CMT nanoparticles show great potential for bimodal image-guided photothermal/immunocollaborative treatment of Rb (Scheme 1).

2. Experimental methods

2.1. Materials and reagents

MIL-100 (Fe) NPs (200 nm) were purchased from Xi'an RUIXI Biological Technology Co., Ltd. (Xi'an, China). Tuftsin was synthesized in NJPeptide (Nanjing, China), and 4′,6-diamidino-2-phenylindole (DAPI), 1,1′-dioctadecyl-3,3,3′,3′-tetramethylindo-carbocyanine perchlorate (DiI), and 3,3′-dioctadecyloxacarbocyanine perchlorate (DiO) were purchased from Sigma-Aldrich Co., LLC (St. Louis, MO). FITC anti-mouse CD16/32 antibody and PE anti-mouse CD206 (MMR) antibody were obtained from Biolegend, Inc. (San Diego, CA). Anti-mouse CD16/CD32 and CD206 antibodies were purchased from Novus Biologicals, LLC (Littleton, CO). The FIX&PERM Kit was purchased from Multi Sciences (LIANKE Biotech, Hangzhou, China). The anti-mouse CD86 antibody was purchased from Affinity Biosciences (Cincinnati, OH). TNF-α enzyme-linked immunosorbent assay (ELISA) kits were obtained from Hunan Aifang Biotechnology Co., Ltd. (Hunan, China). The human RB cell line Y79, human retinal pigment epithelium cell line (ARPE-19), and Ana-1 macrophages were purchased from ATCC (Manassas, VA). Roswell Park Memorial Institute-1640 (RPMI-1640) was acquired from Gibco (Carlsbad, CA). Fetal bovine serum (FBS) was obtained from Bioind (Beit-Haemek, Israel). The Cell Counting
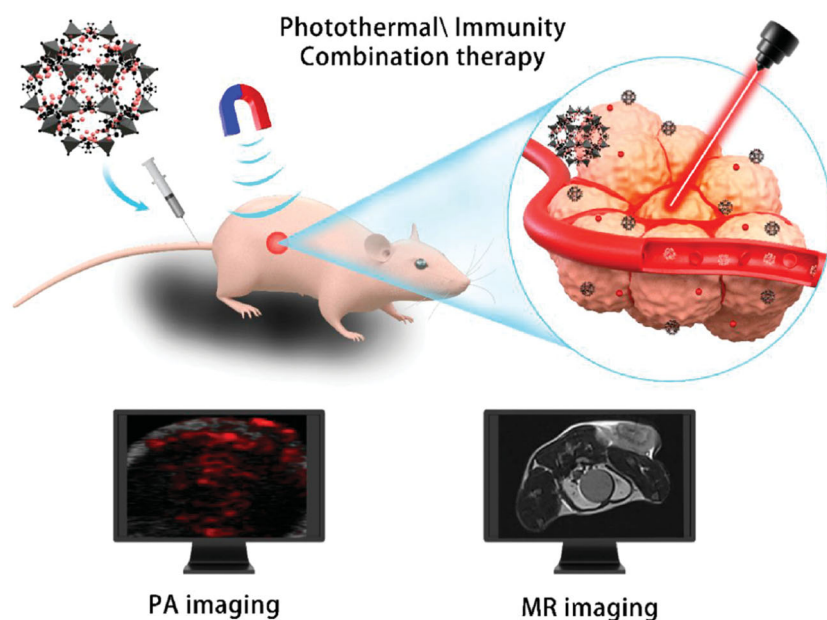
Scheme 1. Photoacoustic and nuclear magnetic imaging of Rb with CMT nanoparticles and a schematic diagram of photothermal combined immunotherapy.

Kit-8 (CCK-8) assay was purchased from Dojindo Laboratories (Kumamoto, Japan).

2.2. Synthesis of CMT NPs

MIL-100 (Fe) NPs were carbonized in a tube furnace under argon atmosphere at high temperature (800 °C, 5 °C/min, 5 h). The obtained CM NPs were pickled with 1 mol/L hydrochloric acid for 48 hours, hydrated with 30% H_2O_2 for 8 h, and then cleaned with PBS three times until the supernatant was neutral. Two hundred micrograms tuftsin and 2 mg CM NPs were added to PBS for mechanical agitation for 24 h, and CM NPs loaded with tuftsin (CMT NPs) were obtained after magnetic separation of absorption in deionized water three times. Then, the samples are cryogenically vacuumed (−50 °C).

In addition, during the preparation of CMT NPs, 100 μg of DiI was added to chloroform and then evaporated at 50 °C for 1 h to label the nanoparticles. The obtained CM NPs were stirred (200 rpm) with 200 μg of tuftsin in PBS for 24 h at 4 °C in the dark. The remaining steps are the same as before. DiI-labeled CMT NPs were obtained. The preparation of DiR-labeled CMT follows the previous steps.

2.3. Characterization

The shape and structure of CMT NPs were characterized by scanning electron microscopy (SEM) (S4000, Hitachi, Chiyoda, Japan). Particle size and zeta potential were measured using a laser particle size analyzer system (Zetasizer Nano, Malvern, UK). The magnetic properties of nanoparticles were measured using a vibrating magnetometer (VSM, Lake Shore 7404, Westerville, OH). The presence of iron in CMT was detected by XRD and XPS. Attenuated total reflection Fourier transform infrared (ATR-FTIR) spectra were detected on an FTIR spectrometer. The standard curve, encapsulation rate, and thermal stability of tuftsin were measured by HPLC

(Waters e2695-2489 UV-Vis Detector, Milford, MA). The tuftsin quantity is measured using the following formula:

$$\text{Encapsulation efficiency } (\%) =$$
$$(\text{weight of tuftsin}/\text{total tuftsin input}) \times 100\%$$

$$\text{Loading capacity } (\%) =$$
$$(\text{weight of tuftsin}/\text{total mass of nanoparticles}) \times 100\%$$

Different concentrations of CMT NPs (100, 200, 400, and 800 μg/mL) were irradiated with an 808 nm laser (2 W/cm^2), and the temperature changes at each time point were recorded by an infrared imager (Fluke Ti32, Gainesville, GA).

2.4. Cell culture

The human Rb cell line Y79, human retinal pigment epithelial cell line (ARPE-19), and Ana-1 macrophages were cultured in RPMI-1640 medium containing 20% FBS and 1% penicillin/streptomycin in an incubator at 37 °C and 5% CO_2. The ARPE-19 cells attached to the wall were assembled and digested with a 0.25% trypsin solution and then subcultured.

2.5. Animal model

Female BALB/C nude mice (4–6 weeks old) were purchased from the Experimental Animal Center of Chongqing Medical University and raised in a suitable environment with sufficient water and food. Y79 cells were suspended in PBS (3×10^6 cells, 100 μL per mouse) and subcutaneously injected into the thighs of nude mice to establish the tumor-bearing mouse model of Y79. All experiments and procedures were carried out in accordance with the guidelinesapproved by the Animal Care and Use Committee of Chongqing Medical University.

2.6. In vitro *cytotoxicity and apoptosis analysis*

ARPE-19 cells and Y79 cells were inoculated in 96-well plates (1×10^4 cells per well) for 24 h and replaced with fresh medium containing different concentrations (100, 200, 400, and 800 μg/mL) of CMT NPs. After incubation for 24 h, 110 μL of fresh medium containing 10% CCK8 working solution was added. Then, the absorbance of each well at 450 nm was measured with a microplate reader (EL $\times$ 800 Universal Microplate Reader, BIO-TEK Instrument, Winooski, VT).

In the *in vitro* treatment experiment, Y79 cells were inoculated on a 24-well plate for 24 h and were treated as follows: control group, tuftsin only, laser only, CMT NPs only, laser + CM NPs, and laser + CMT NPs ($n = 3$). Then, the prompt group was treated with a 1.5 W/cm^2 laser for 5 min. Y79 cells were inoculated into 24-well plates (5×10^4 cells per well) for 24 h and treated accordingly. FITC-Annexin V and propidium iodide (PI) (BD Biosciences, San Jose, CA) were stained according to the instructions and analyzed by flow cytometry. To further observe the cell apoptosis and necrosis induced by CM/CMT NPs under laser irradiation.

2.7. In vitro *detection of macrophage type*

Macrophages were inoculated on 24-well plates (5×10^4 cells) and grouped as tuftsin only, laser only, CMT NPs only, laser + CM NPs, and laser + CMT NPs ($n = 3$). After 48 hours, the treated cells were collected, and anti-mouse FITC-labeled CD16/CD32 antibody was added. After 30 min of incubation at 4 °C, the membrane was disrupted using a FIX&PERM Kit according to the instructions, and an anti-mouse PE-labeled CD206 antibody was added. Finally, the macrophage type was detected by flow cytometry.

2.8. *Magnetic targeting ability*

Y79 cells were inoculated into 6-well plates (2×10^5 cells per well), and a predetermined amount of DiI-labeled CMT NPs was added. The magnet (approximately 1 T) was next to the hole, and an additional set of cells was incubated for 0, 1, 2, 4, and 8 h. After the nanoparticles and cells were incubated, the culture medium was removed by centrifugation, and 1 mL 4% paraformaldehyde was added for fixation for 10 min, followed by DiO staining for 15 min. The excess DiO was removed by PBS centrifugation, followed by 100 μL DAPI staining for 10 min. Finally, PBS was used for centrifugal cleaning and detection. Intracellular uptake of CMT NPs near the magnet (target area) and away from the magnet (control area) was observed using CLSM to detect the magnetic targeting properties of CMT NPs, and flow cytometry was used to quantitatively analyze the intracellular uptake of DiI-labeled CMT NPs at different times.

Ten Y79 tumor-bearing nude mice were randomly divided into two groups ($n = 5$): the DiR-labeled CMT NP group under magnetic field treatment and the DiR-labeled CMT NP group without magnetic field treatment. First, mice in both groups were injected with DiR-labeled CMT NPs (200 μL, 2 mg/mL) via the tail vein. Then, a magnet (approximately

1 T) was placed on the tumor, and fluorescence images were obtained at different times (0, 1, 2, 4, 8, and 24 h) after the injection of nanoparticles through fluorescence lines. The tumor and main organs of mice were collected for fluorescence imaging, and the corresponding fluorescence signal was calculated.

2.9. In vitro *and* in vivo *dual-modal imaging*

The ability of CMT NPs as a PA imaging contrast agent was tested by an AGAR gel module, and the ability of CMT NPs as an MR imaging contrast agent was tested by an EP tube. PA images and PA values of the six groups (100, 200, 400, and 800 μg/mL CMT NPs; 800 μg/mL CM NPs; saline) were recorded and analyzed by a VEVO LASR imaging system (Toronto, Canada). CMT NPs were dispersed in doubly distilled water at different concentrations (5, 10, 20, 40, and 80 μg/mL), added to an EP tube and placed in a nuclear MR instrument to collect MRI images. Sante DICOM Viewer (Santesoft, Cyprus, Athens, Greece) was used to analyze signal strengths (SI) in the region of interest (ROI). The T2WI parameters were set as follows: the repetition time (TR) was 8000 ms, the echo time (TE) was 85 ms, the slice thickness was 1.50 mm and a 3.0 T Siemens MRI scanner was used.

Dual-modal imaging experiments were performed on Y79 tumor-bearing mice *in vivo*. The tumor-bearing mice were divided into three groups (CMT NPs, CM NPs, and saline) ($n = 3$). After the nanoparticles were injected into the tail vein of nude mice (200 μL, 2 mg/mL), a magnetic field was applied to the tumor area, and the corresponding PA images and PA values at different time points (0, 1, 2, 4, 8, and 24 h) were recorded by the VEVO LASR imaging system. The corresponding MR images were simultaneously recorded by the SIEMENS 3.0T TX MR Scanner at different time points (0, 1, 2, 4, and 8 h), and the SI of the ROI was analyzed using the Sante DICOM Viewer (Santesoft, Cyprus, Athens, Greece).

2.10. In vivo *therapy*

When the tumor volume of the tumor-bearing mice reached 0.8 cm^3, the mice received different treatments (control group, tuftsin only, laser only, CMT NPs only, CM NPs + laser, and CMT NPs + laser) ($n = 5$). The control group was injected with 200 μL normal saline through the tail vein. After injection of the nanoparticles (200 μL, 2 mg/mL), a magnetic field was applied to the tumor area for 4 h, followed by irradiation of the tumor with a 1.5 W/cm^2 laser for 5 min. The body weights and tumor volumes of the nude mice were recorded every two days. Tumor volume was defined as volume (mm^3) $V = \pi/6 \times L \times W^2$.

After the nude mice were treated for a predetermined time, the tumors were divided into two parts. The first part was fixed with 4% paraformaldehyde, followed by hematoxylin–eosin (H&E) staining, proliferating nuclear antigen (PCNA), and TDT-mediated nickel end labeling of dUTP (TUNEL). All section images were obtained using the same microscope (Olympus Corp., Shinjuku, Japan) and camera (Olympus Corp., Shinjuku, Japan). Five regions were randomly read at

×200 magnification, and the percentage of positive cells in the total number of cells was calculated. The second part was homogenized at 4 °C. Western blotting (WB) and ELISA were used to detect whether CMT NPs combined with laser irradiation could induce macrophages to transform into the M1-type and achieve effective immune activation. Proteins were extracted from each sample as instructed and separated by 10% gel SDS-PAGE electrophoresis, followed by electrical transfer to a polyvinylidene fluoride membrane. After encapsulation with 5.0% skim milk powder and Tris-buffered saline (1× TBS), they incubated with primary antibodies targeting CD86 (1:1000) at 4 °C for 12 h followed by the appropriate specific secondary antibodies (1:10,000) for 1 h. The immune reaction band was observed with chemiluminescence substrate according to the manufacturer's instructions. Protein bands were normalized to β-actin bands, and all imprints were quantified using Image Lab software (Bio-Rad Laboratories, Hercules, CA). For ELISA, TNF-α kits were used according to the manufacturer's instructions.

2.11. In vivo biocompatibility studies

H&E staining was performed on the main organs of nude mice after the above treatment to evaluate the biosafety of the laser combined with CMT NPs in vivo. Twenty female nude mice were injected with 200 μL of different solutions (saline and 2 mg/mL CMT NPs) through the tail vein, and their body weight was recorded every two days. Blood samples (0.8 mL) were collected 1, 7, and 14 days after injection of CMT NPs for routine blood tests and liver and kidney function tests.

2.12. Statistical analysis

All statistical analyses were performed with Statistical Package for GraphPad 8.0 software (GraphPad Inc., Chicago, IL) and Origin 2021 (OriginLab, Massachusetts, US). Comparisons between two groups were assessed with the t-test, and one-way analysis of variance (ANOVA) was applied for comparisons among groups. Repeated measures of ANOVA were used in analyses at different time points. Statistical significance was defined as $*p < .05$, $**p < .01$.

3. Results and discussion

3.1. Synthesis and characterization of CMT

CMT is a unique magnetic carbonized nanoparticle. Mil-100 (Fe) was carbonized at high temperature to obtain magnetic and carbon-specific CM NPs, which were mechanically stirred and successfully encapsulated with tuftsin. Therefore, CMT can be used for bimodal imaging of tumors and laser/immunotherapy. Due to its magnetic targeting and EPR effect, CMT NPs can easily be transported through blood vessels and accumulate in tumors, reducing drug hydrolysis and increasing drug concentration at the tumor site (Wu & Yang, 2017; Wang et al., 2018; Haimov-Talmoud et al., 2019). Its magnetic and carbon optical properties make it an MR/PA imaging contrast agent (Chen et al., 2014; Song et al., 2020). Under laser irradiation, the temperature of the irradiation area increases, which not only exerts a mild photothermal treatment effect but also induces macrophages to transform into the M1-type by releasing tuftsin, which helps to improving the tumor microenvironment and activating immunotherapy.

The constructed multifunctional CMT NPs were synthesized as shown in Figure 1.

Multifunctional CMT NPs were prepared by carbonization, acidification, hydration, and mechanical agitation. This method has been mastered and successfully applied in previous studies, with uniform particle size (Figure 2(B)) (Xia et al., 2013). The particle size of MIL-100 (Fe) was 265.7 ± 105.4 nm (Figure 2(C)) and that of CMT NPs was 303.1 ± 48.53 nm (Figure 2(D)), which was consistent with the SEM characterization. The particle size of nanoparticles changed due to the influence of carbonization temperature (Huo et al., 2017). In tumor tissues, due to the lack of vascular supporting tissue, leaky blood vessels and capillary pores are easily formed. Nanoparticles of appropriate size (100 nm to 2 μm) can passively accumulate in tumor tissues, which is called the EPR effect (Wu et al., 2018). CMT NPs have good EPR effect conditions. The zeta potential of MIL-100 (Fe) was 28.4 ± 4.38 mV and that of CMT NPs was −12.1 ± 2.88 mV (Figures S1 and S2). According to the hysteresis curve results (Figure 2(E,F)), MIL-100 (Fe) has no magnetic properties, while CMT NPs have good magnetic properties, resulting in good conditions for magnetic targeting capability and MRI imaging in the future (Chen et al., 2014).

Figure 3(A) shows the XRD patterns of Fe_3O_4, FeO, and graphite. According to JADE 9 peak search, diffraction peaks appear at 2θ at 26.563°, 34.220°, 43.113°, 56.165°, 63.746°, and 74.052°. After JADE 9 search, it was found that the XRD pattern was basically consistent with the position and intensity of the characteristic peak of the standard card of Cubic Fe_3O_4 (JCPSD 76-0956), and the crystal plane index of corresponding Fe_3O_4 was (113), (121), (220), (231), (2010), and (416). CMT can be confirmed to contain Fe_3O_4. After JADE 9 peak search, it can be seen that the diffraction peaks are 41.573°, 60.249°, and 72.103° at 2θ. After JADE 9 search, it can be found that the XRD pattern is basically consistent with the position and intensity of the characteristic peaks of the cubic FeO (JCPSD 74-1886) standard card. The crystal plane index of
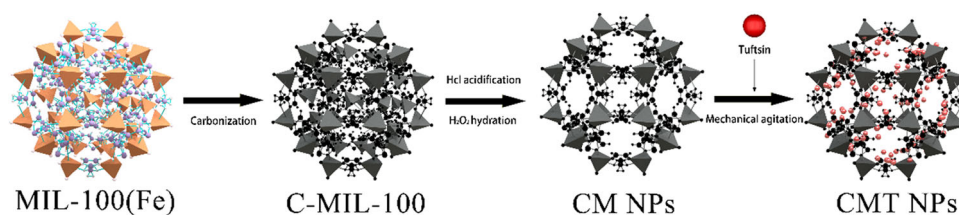

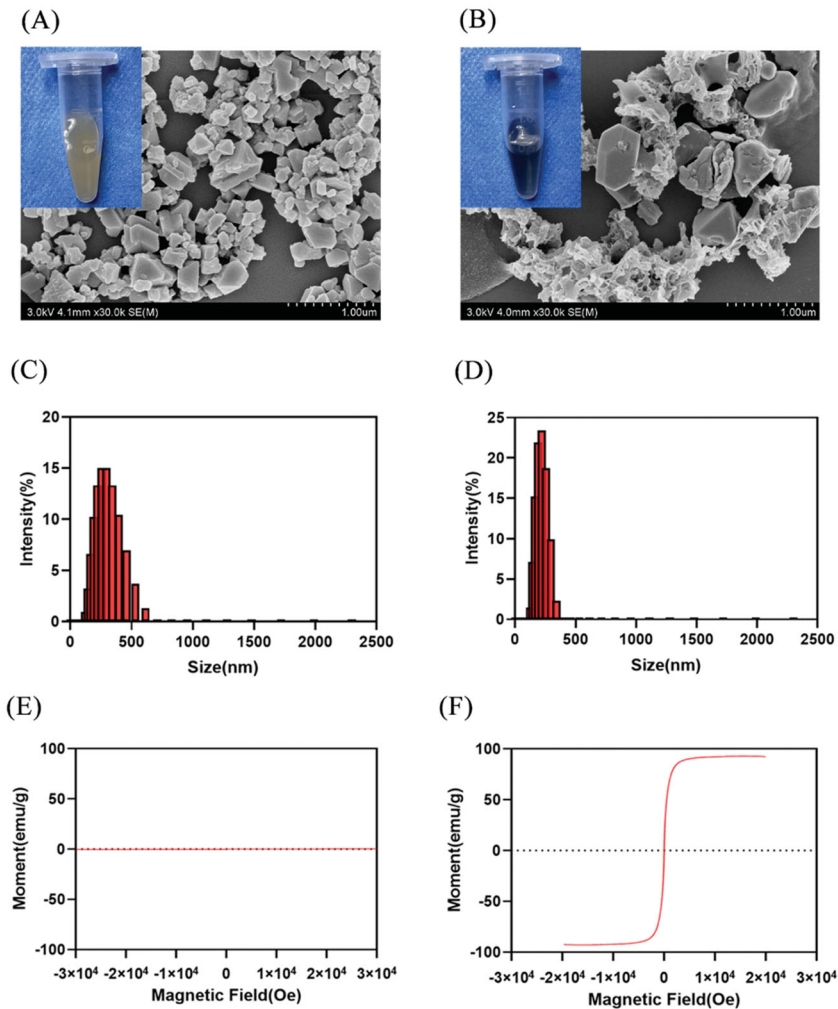Figure 1. Preparation process of CMT NPs.

(A)

(B)

(C)

(D)

(E)

(F)

Figure 2. (A, B) Scanning electron microscopy (SEM) images and test tube images of MIL-100 (A) and CMT NPs (B). (C, D) The particle size distribution of MIL-100 (C) and CMT NPs (D). (E, F) Hysteresis curve of MIL-100 (E) and CMT NPs (F).

corresponding FeO is (200), (220), and (311), which can confirm that CMT contains FeO. After JADE 9 peak search, it can be seen that at 2θ 26.554° diffraction peak, after JADE 9 search found that the XRD pattern and cubic graphite (JCPSD 89-8487) standard card characteristic peak position and strength are basically consistent, corresponding to the graphite crystal plane index is (002), CMT can be confirmed to contain carbon.

As shown in Figure 3(B), the binding energies of Fe^{2+}, Fe^{3+}, and Fe^{2+} in CMT are 709.82 and 722.83, and those of Fe^{3+} are 710.89 and 724.69.

The Fourier infrared absorption spectrum of Mil-100 (Fe) after carbonization changed obviously, indicating that the material was carbonized successfully (Figure 3(C)). In addition, when CMT NPs are compared with CM NPs, the characteristic band of CMT NPs at 3446 CM^{-1} corresponds to O–H stretching of Tuftsin, indicating that Tuftsin is loaded into CMT NPs (Figure 3(D,E)). The regression equation of tuftsin standard curve obtained from HPLC results is $Y = 12,200X - 34,995$, $R^2 = 0.9991$ (Figure 3(F)). According to the formula and the regression equation of standard curve, the encapsulation rate and drug loading rate are $29 \pm 4.09\%$ and $2.64 \pm 0.37\%$, respectively. Thermal stability of tuftsin: at different temperatures (Figure 3(G)), there was no statistically

significant difference in the peak area of tuftsin performance liquid phase ($p > .05$).

3.2. Photothermal conversion capacity

Under irradiation with an 808 nm laser, the temperature of the CMT NP suspension with different concentrations (100, 200, 400, and 800 µg/mL) increased with increasing laser irradiation time. The higher the concentration of CMT NPs was, the higher the temperature (Figure 4(A)). The temperature of 800 µg/mL nanoparticles irradiated with a 2 W/cm² laser for 180 s reached 57.5 °C (Figure 4(B)), indicating that CMT has good photothermal conversion ability and is an ideal photothermal treatment material. The laser on–off experiment of CMT shows that CMT has stable photothermal conversion capability (Figure 4(C)). After calculation, the photothermal conversion efficiency of CMT is 27.08%. The photothermal conversion efficiency of gold nanorods is about 30% (Liu et al., 2020), and the photothermal conversion efficiency of gold-based composites is up to 50% (Zhang et al., 2021). The photothermal conversion capability of CMT NPs has some limitations, but it still has broad prospects in the field
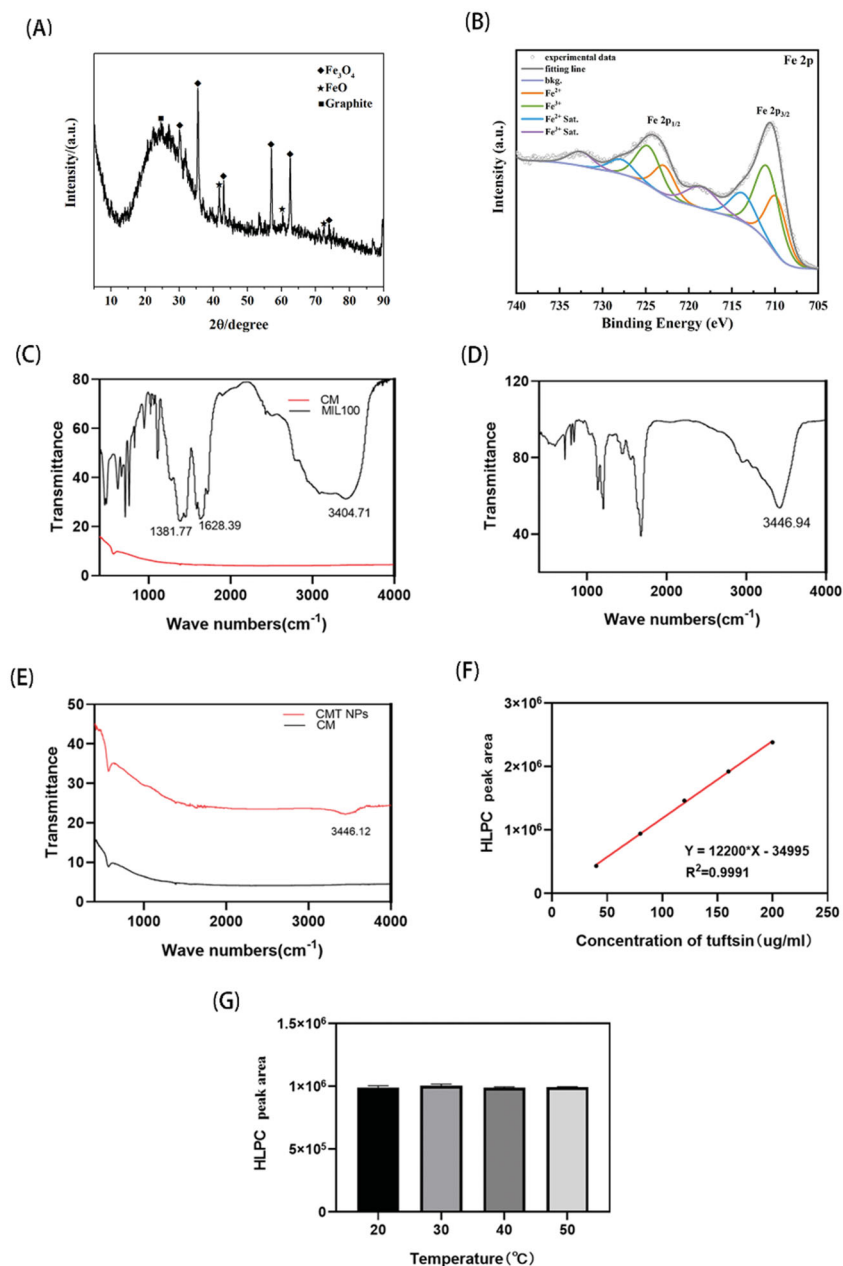
(A)

(B)

(C)

(D)

(E)

(F)

(G)

Figure 3. (A) XRD of CMT NPs; (B) XPS of CMT NPs; (C) Fourier transform infrared spectroscopy (FTIR) of MIL-100 (Fe) and CM NPs; (D) Fourier infrared spectroscopy of tuftsin; (E) infrared spectra of CM and CMT NPs; (F) HPLC standard curve of tuftsin; (G) peak area of tuftsin at 20, 30, 40, and 50 °C ($p > .05$).

of mild PTT, and its cost is lower than that of gold nanomaterials, which has unique advantages.

3.3. In vitro *analysis of cytotoxicity and apoptosis*

ARPE-19 cells were cultured with different concentrations of CMT (100, 200, 400, and 800 μg/mL) for 24 h, as determined by CCK-8 assay. Even at 800 μg/mL, the viability of the cocultured cells was excellent (Figure S3), indicating that CMT NPs are biologically safe and thus has the potential for further application in biomedicine. To further observe the apoptosis and necrosis induced by CMT NPs under laser irradiation, cells stained with FITC-Annexin V and PI were detected by flow cytometry (Figure 5(A,B)). As shown in the figure, under laser irradiation, the CM and CMT NPs groups were

significantly higher than the single laser group, indicating that after adding CM and CMT materials, laser energy could be converted into heat energy, resulting in thermal damage to cells (Zhi et al., 2020). Importantly, there was no significant difference in cell viability between cells loaded with tuftsin and those not loaded with tuftsin in the nanoparticle-treated cells. Tuftsin did not kill tumor cells directly *in vitro* without macrophages; tuftsin can bind macrophages through specific receptors, activate macrophages through activation of the NF-kB pathway, and induce their differentiation into M1 cells, while M1 macrophages can secrete TNF-α, NO, IL-12, and other cytokines to induce tumor cell apoptosis (An et al., 2014; Guerra et al., 2017). Consistent with the CCK-8 results, laser combined with CM or CMT NPs induced more apoptosis in Y79 cells, while laser and tuftsin treatment did not affect cell viability. The photothermal effect of the laser
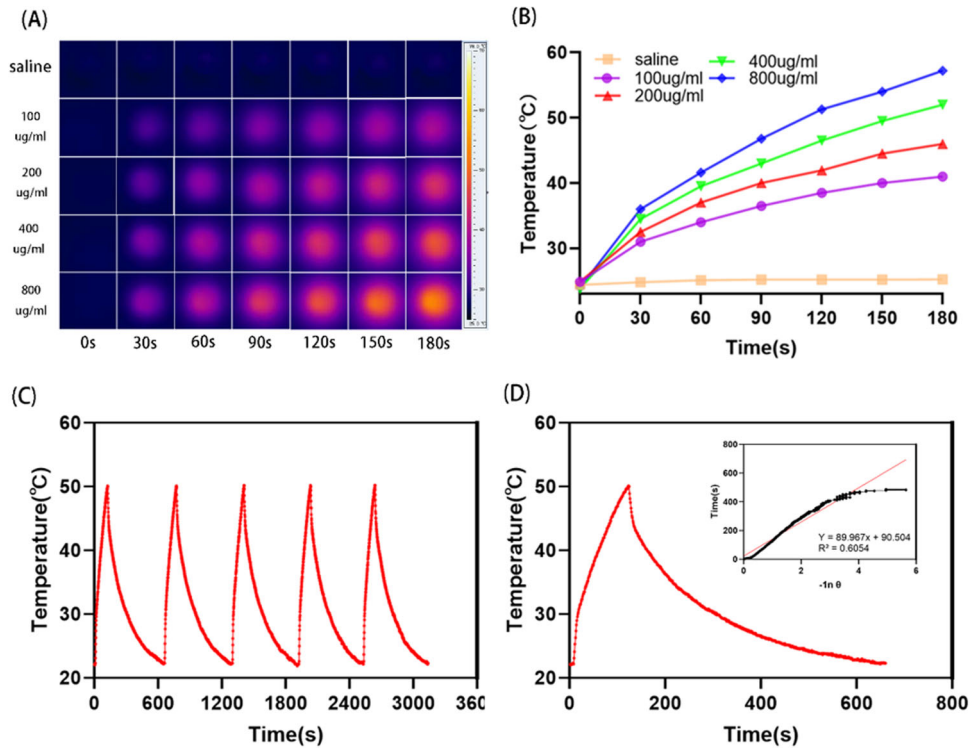
Figure 4. (A) Temperature change images of different concentrations of CMT NPs (100, 200, 400, and 800 μg/mL) at different time points under 808 laser excitation. Data statistics are shown in (B). (C, D) Laser on-off experiments of CMT nanoparticles. Linear of temperature and time is shown in (D).
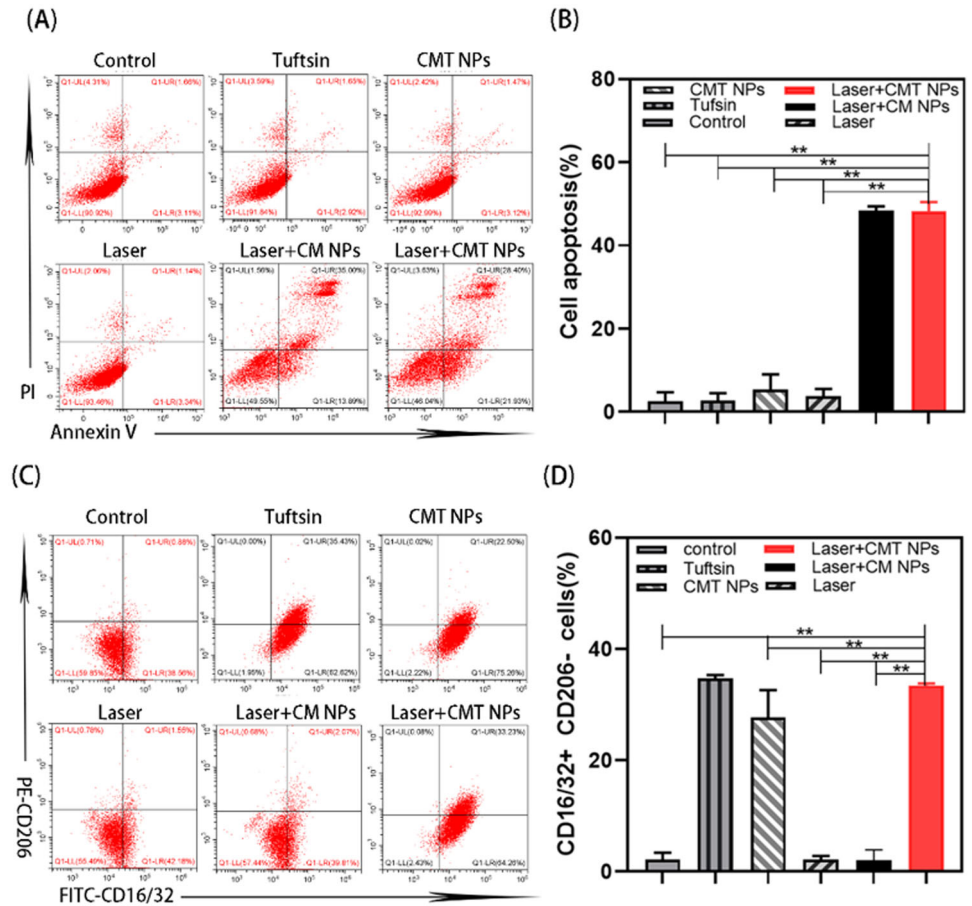

Figure 5. (A, B) Flow cytometry was used to analyze the apoptosis of Y79 cells after different treatments (control, tuftsin only, laser only, CMT NPs only, CM NPs + laser, CMT NPs + laser). (C, D) Flow cytometry analysis of CD16/32 and CD206 expression in Ana-1 macrophages after different treatments (**$p < .01$).

may be the main influencing factor in the *in vitro* cytotoxicity study, which leads to cell division or necrosis. This also explains why only the laser combined group and the CM or CMT NPs group had relatively high apoptosis rates.

3.4. Typing detection of macrophages

After different treatments, tuftsin stimulated macrophages to differentiate into the M1 type, and the expression of CD16/32 and CD206 was detected by flow cytometry. After laser irradiation, the proportion of CD6/32-positive cells in the CMT NPs group was as high as $33.13 \pm 0.23\%$ (Figure 5(C,D)), close to the level of tuftsin-treated cells. *In vitro* studies showed that tuftsin directly promoted the transformation of macrophages into the M1 type, but *in vivo* studies showed that tuftsin had difficulty acting on macrophages at the

tumor site. There was no significant difference in CD16/32 expression between the control group and the group without tuftsin treatment, indicating that laser and CM nanoparticles could not induce macrophage typing alone. Therefore, these data suggest that laser irradiation of CMT NPs induces macrophage differentiation.

3.5. Magnetic targeting capability

The more nanoparticles accumulate in the tumor and the higher the drug concentration is, the better the treatment effect is. Therefore, we designed and conducted *in vitro* experiments to detect the magnetic targeting properties of CMT nanoparticles. The ability of DiI-labeled CMT NPs to accumulate in Y79 cells under an *in vitro* magnetic field was verified by CLSM. The intracellular uptake of CMT NPs near the magnet (target) was observed with a magnet of
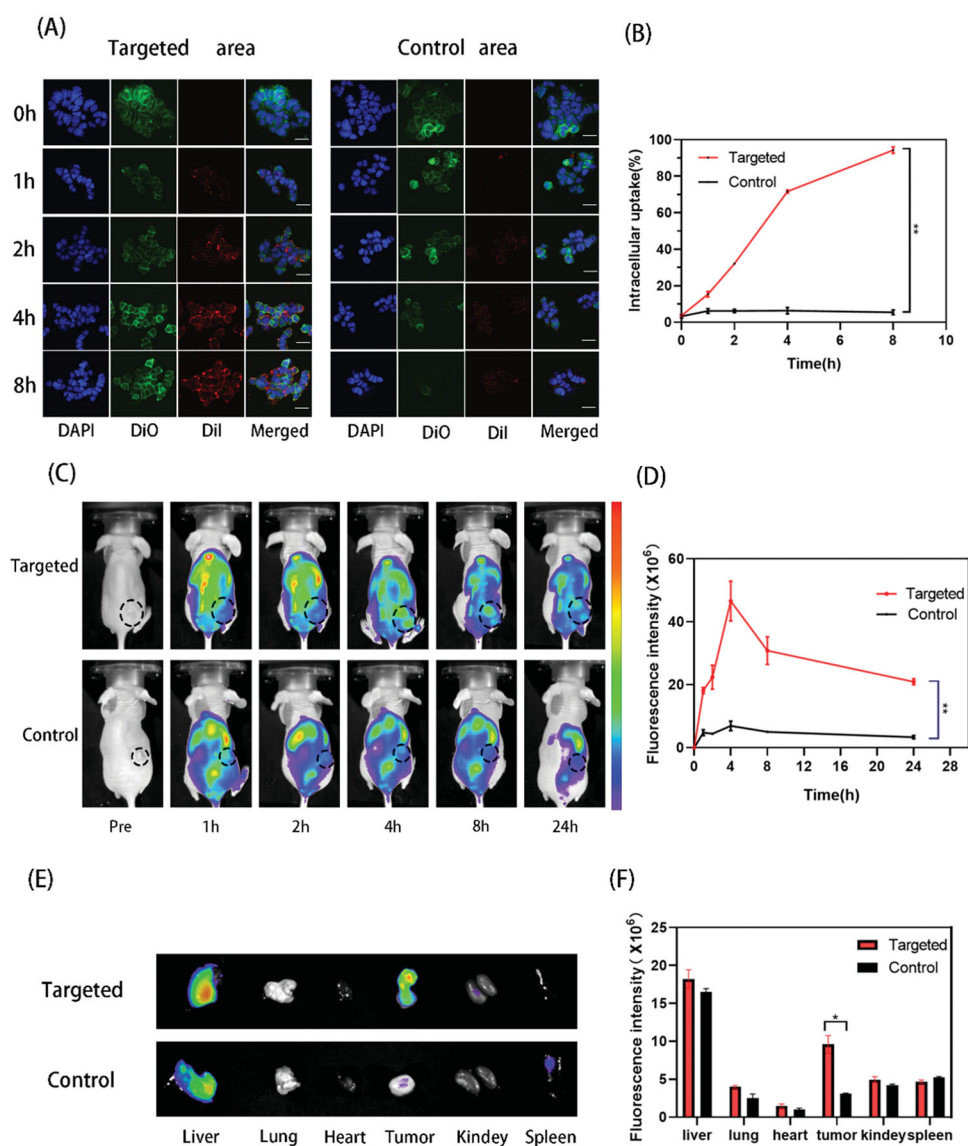

Figure 6. (A) CLSM images of Y79 cells and CMT NPs cocultured under a magnetic field for 0, 1, 2, 4, and 8 h (DiI-labeled CMT NPs, DAPI-labeled Y79 nucleus and DiO-labeled cell membrane). The scale bar is 50 μm. (B) Flow cytometry analysis of the intracellular uptake of DiI-labeled CMT NPs. (C) *In vivo* fluorescence imaging was performed, and CMT NPs fluorescence signals were observed 0, 1, 2, 4, 8, and 24 h after injection. (D) Fluorescence quantitative intensity of tumors 0, 1, 2, 4, 8, and 24 h after injection. (E) Biological distribution of DiR-labeled CMT NPs in major organs and tumors of mice 24 h after injection. (F) Fluorescence quantitative intensity of major organs and tumors (*$p < .05$, **$p < .01$).

approximately 1 T attached to one side of the pore plate and was compared with that in a weaker magnetic field (control). The cell membrane and nucleus of Y79 cells were labeled with DiO green fluorescence and DAPI blue fluorescence, respectively, and CMT NPs were labeled with red. In addition, the intracellular quantitative uptake of fluorescently labeled CMT at different times was analyzed by flow cytometry. As shown in Figure 6, there was no significant difference in the intracellular uptake of nanoparticles between the target area and the control area at 0 h of incubation. However, the uptake of nanoparticles in the target cells increased gradually with time. At the same time, only a small number of nanoparticles existed around cells in the control area at each time point. Endocytosis may play an important role in the uptake and accumulation of nanoparticles (Donahue et al., 2019). Therefore, the results showed that the concentration of CMT NPs in the target area increased significantly under the magnetic field, effectively increasing the concentration of tuftsin and thus improving the efficacy.

To further verify the magnetic targeting of nanoparticles in vivo, we injected DiR fluorescence-labeled CMT NPs into Y79 tumor-bearing nude mice and conducted fluorescence imaging at long time points. As shown in the figure, a strong time-varying fluorescence signal was detected in the tumor region under the action of a magnetic field. After the injection of nanoparticles, the fluorescence intensity in the tumor region increased at 1 h and reached the maximum value at 4 h. After that, the fluorescence intensity gradually decreased, and there was still a fluorescence signal in the 24h tumor region. In the control group, a short-term weak fluorescence signal appeared in the tumor area, which may be related to the EPR effect of nanoparticles (Jian et al., 2014). To explore the biological distribution of CMT NPs in vivo, fluorescence imaging was performed on major organs and tumors (Figure 6(E)), and the corresponding fluorescence intensity was quantified by a fluorescence analysis system (Figure 6(F)). The accumulation of CMT nanoparticles in the liver and spleen of the two groups was due to phagocytosis of the reticuloendothelial system, which is the normal physiological pathway of nanoparticle metabolism in vivo (Overchuk & Zheng, 2018). The fluorescence imaging trends of in vivo and in vitro tissues were consistent. The tumors in the magnetic field irradiation group had a fluorescence signal, while the tumors in the nonmagnetic field irradiation group had almost no fluorescence signal. The results showed that CMT NPs could accumulate effectively in tumor tissue for a long time without damaging major organs under the action of a magnetic field. In this study, the magnetism of CMT NPs plays an indispensable role. After carbonization, CMT NPs become superparamagnetic and accumulates rapidly and efficiently in tumors under the action of a magnetic field. Although active targeted particles produced by specific antibodies are widely used in many fields, their role is limited due to the differences in specific antibodies produced by different types of tumors and the limited role of antibodies in complex environments in vivo (Cheng et al., 2021). Therefore, CMT NPs can be applied to a variety of tumors, not only ophthalmological ones.

3.6. Multimodal imaging in vitro and in vivo

To investigate whether CMT NPs have the required properties for PA imaging, nanoparticles were first scanned in the full spectral range of 680–960 nm. We found that the strongest wavelength of the PA signal of CMT was approximately 710 nm (Figure S4), so this wavelength was selected as the best excitation wavelength for subsequent experiments. As shown in Figure 7(A,B) and PA mode, in the range of 100–800 μg/mL, the signal is enhanced with increasing CMT NPs concentration, indicating that the nanoparticles have good PA performance. The regression equation is $Y = 0.002132 \times X + 0.07742$, $R^2 = 0.9857$ (Figure 7(C)). Moreover, at the same concentration of 800 μg/mL, CM also had good PA performance. Subsequently, PA imaging was performed on tumor sites of Rb mouse models injected with CMT NPs, CM NPs and normal saline at different times according to in vitro experimental results (Figure 7(D)), and PA values were quantitatively analyzed (Figure 7(E)). After the injection of CMT and CM NPs, the tumor PA signal increased gradually at 1 h and reached a peak at 4 h. With the metabolism of nanoparticles, the accumulation in the tumor gradually decreased. It is worth noting that although the PA value was reduced, there were still obvious PA signals at 8 h and even 24 h. Therefore, CMT NPs are expected to be an ideal PA imaging agent for imaging-guided tumor therapy.

To further explore whether CMT NPs have the required properties for MR imaging, we performed T2WI MR imaging on CMT NPs. As shown in the figure, CMT NPs negatively enhance T2WI MR imaging, and SI decreases with increasing concentration. In addition, there is a good linear relationship between $1/T_2$ and the CMT NPs concentration. The
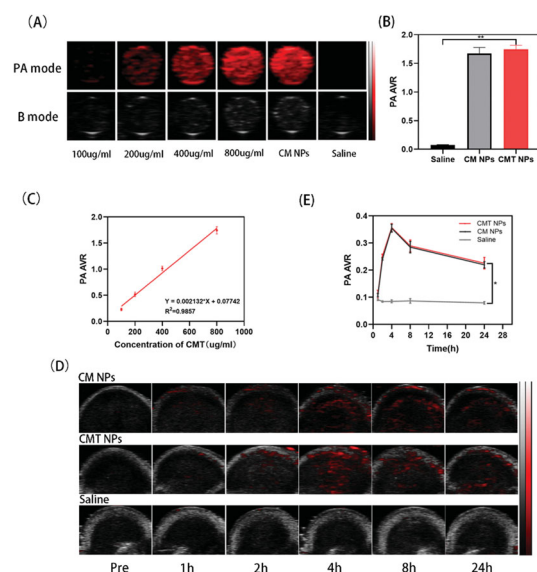

Figure 7. (A) PA images of CMT NPs (100, 200, 400, and 800 μg/mL), CM NPs (800 μg/mL), and normal saline. (B) PA values of CMT NPs (800 μg/mL), CM NPs (800 μg/mL), and normal saline. (C) PA values of CMT NPs (100, 200, 400, and 800 μg/mL). (D) Tumor PA images of Y79 tumor-bearing mice after intravenous injection of CMT NPs, CM NPs, and normal saline at different times. (E) Tumor PA value of Y79 tumor-bearing mice at the corresponding time point (*p < .05, **p < .01).
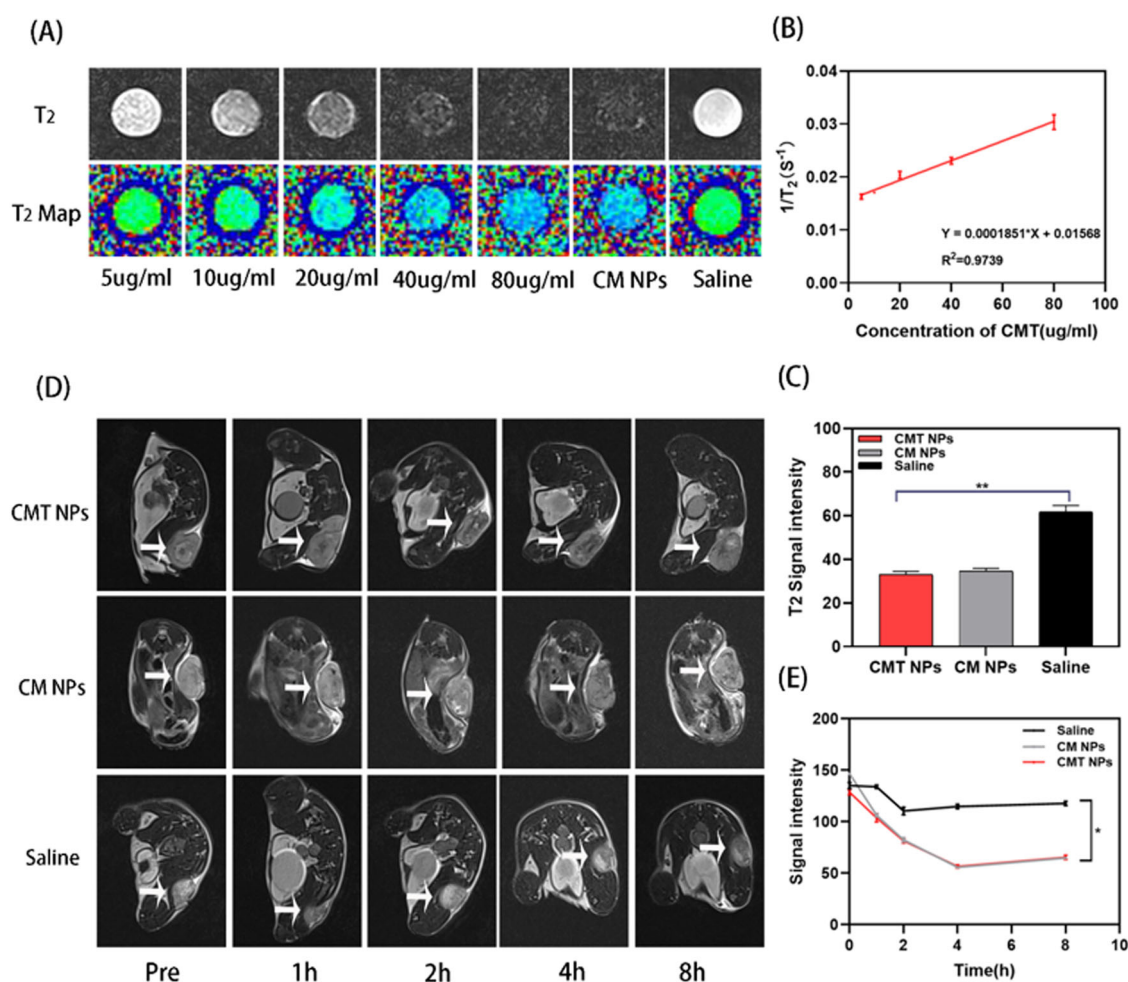
Figure 8. (A) T2WI MRI of CMT NPs (5, 10, 20, 40, and 80 μg/mL), CM NPs (80 μg/mL), and normal saline. (B) SI of CMT NPs in T2WI MR imaging (5, 10, 20, 40, and 80 μg/mL). (C) Signal intensity of CMT NPs (80 μg/mL), CM NPs (80 μg/mL), and normal saline in T2WI MRI. (D) T2WI MR imaging of Y79 tumor-bearing mice injected with CMT NPs, CM NPs, and normal saline at different times. The arrow represents the tumor. (E) T2WI MR imaging showed the corresponding signal intensity of tumors in Y79 tumor-bearing mice ($*p<.05,**p<.01$).

regression equation is $Y = 0.0001851 \times X + 0.01568$, $R^2 = 0.9739$ (Figure 8(B)). Subsequently, based on the results of *in vitro* studies, the imaging ability of CMT as a T2WI MR imaging contrast agent in Y79 tumor-bearing mice was further studied. The SI of the tumor decreased gradually at 1 h, as shown in the figure. In the CMT and CM NPs groups, SI reached its lowest level at 4 h after intravenous injection of nanoparticles, with significant negative enhancement of nanoparticle concentration and SI in body tissues. In conclusion, CMT and CM NPs can enhance the SI difference between tumor and normal tissue and contribute to tumor diagnosis. However, saline did not cause this effect. T2WI MR imaging and quantitative results showed that SI and saline did not change significantly with time. These results indicate that CMT nanoparticles not only possess magnetic targeting properties but also can negatively enhance T2WI MR imaging. In summary, CMT NPs have the characteristics required for dual-mode imaging.

3.7. In vivo *therapy*

Laser irradiation is an effective, safe, and noninvasive treatment for cancer (Lee et al., 2016). CM NPs, CMT NPs, and saline were injected through the caudal vein. After the magnetic field was applied for 4 h, laser irradiation (1.5 W/cm^2, 3 min) could make the temperature in the tumor area reach 45 °C (Figure 9(A,B)), confirming the effectiveness of photothermal conversion *in vivo* and realizing PTT. Immunotherapy has become a topic of intense interest in cancer treatment. The effective combination of immunotherapy and nanoparticles provides a new direction for tumor treatment (Chen et al., 2016, 2019; Riley et al., 2019). The *in vitro* treatment of Y79 cells by laser combined with CMT NPs provides a basis for further study *in vivo*. The results of testing the *in vivo* efficiency of the laser combined with CMT NPs is shown in Figure 9(C). Tumor volume decreased gradually in the laser + CMT NPs group. In the other groups, the treatment was less effective, or the tumor grew again. After different treatments, the tumor was excised. Relative tumor volume (V/V_0) curves during the observation period are shown in Figure 9(D). The tumor volume of the laser + CMT NPs group decreased gradually, and the therapeutic effect was significantly better than that in the other groups. As expected, the laser + CMT NPs group had the highest rate of tumor volume suppression.
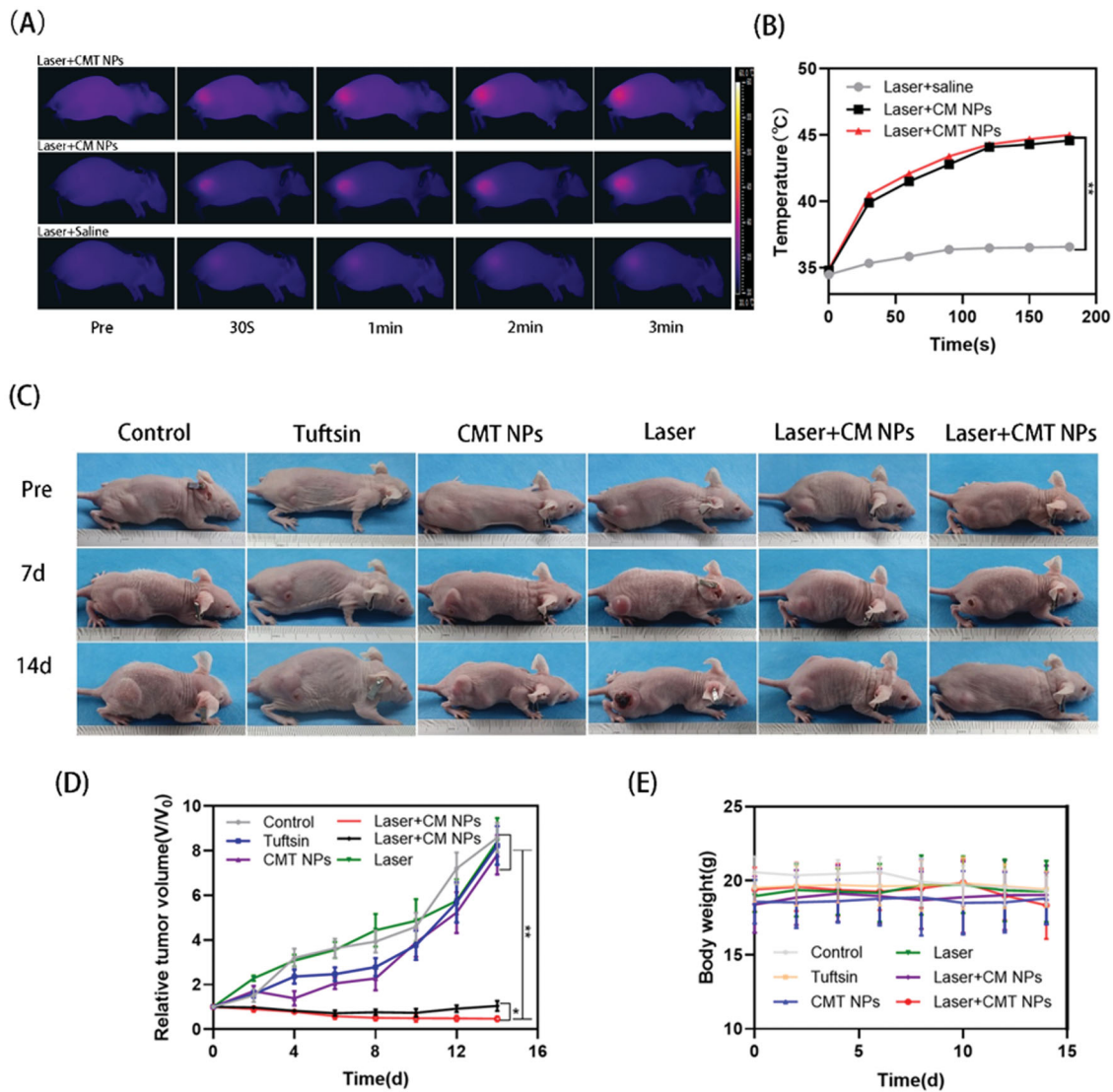
Figure 9. (A) Thermal images of tumor-bearing mice 4 h after injection of CM NPs, CMT NPs, and saline under laser irradiation (1.5 W/cm², 3 min). (B) Temperature–time curves of the three groups. (C) Photos of six groups of Y79 tumor-bearing mice at 14 days after different treatments. (D) Relative tumor volume (V/V_0) curve with time. (E) Body weight of Y79 tumor-bearing nude mice at 14 days ($n = 5$, *$p<.05$, **$p<.01$).

H&E, TUNEL, and PCNA staining of tumor slices further verified the efficacy of laser combined with CMT NPs (Figure 10(A)). H&E staining showed that tumor cell necrosis was significantly higher in the laser + CMT NPs group than in the other groups. TUNEL and PCNA also showed similar trends. The apoptosis index was the highest and the proliferation index lowest in the laser + CMT NPs group (Figure 10(B,C)). These histological results showed that laser combined with CMT NPs had the best efficacy, significantly better than that of the other groups. To test the differentiation of macrophages and the effect of immunotherapy in vivo, the tumor was homogenized with WB and ELISA. After 14 days of treatment, the levels of CD86 and TNFα in laser + CMT NPs group were significantly different from those in other groups (Figure 11(A,B)). CD86 has a high expression level in M1-type macrophages, which is often used as a marker to identify macrophage typing (Lu et al., 2018; Väyrynen et al., 2021), and the increased expression of CD86 suggests that laser + CMT NPs can successfully induce M1-type polarization

of macrophages. At the same time, we noted that tuftsin was the key to inducing immune effect, so CD86 in tuftsin only and CMT NPs only groups increased compared with the control group. From the results, the encapsulation of nanoparticles and laser intervention improved the efficiency of drug action. In addition, M1 is characterized by the expression of a large number of induced cytokines such as TNF-α and NO, and by promoting pro-inflammatory and immune responses to exert anti-tumor activity (Gerspach et al., 2009; Chanmee et al., 2014; Qiu et al., 2022). The results of WB and ELISA showed that laser + CMT NPs could effectively induce macrophage typing, providing a new idea and a favorable platform for tumor immunotherapy.

3.8. In vivo biocompatibility studies

First, the weight of the mice was recorded every two days, with very little fluctuation (Figure S5). Then, the blood biochemistry and complete blood analysis of the mice were
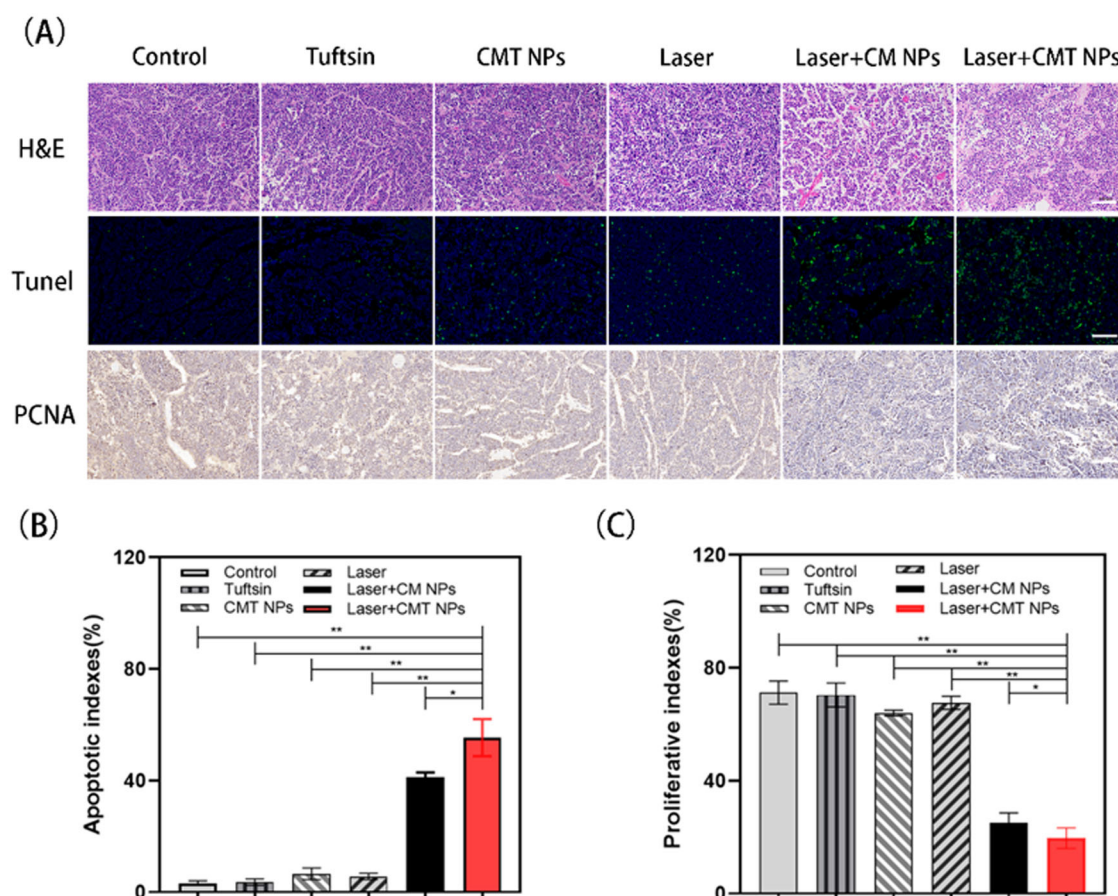
Figure 10. (A) Tumor sections after different treatments were stained with H&E, TUNEL, and PCNA. The scale bar is 50 μm. (B) Apoptosis indexes of Y79 tumors after different treatments. (C) Proliferation indexes of Y79 tumors after different treatments (*$p<.05$, **$p<.01$).
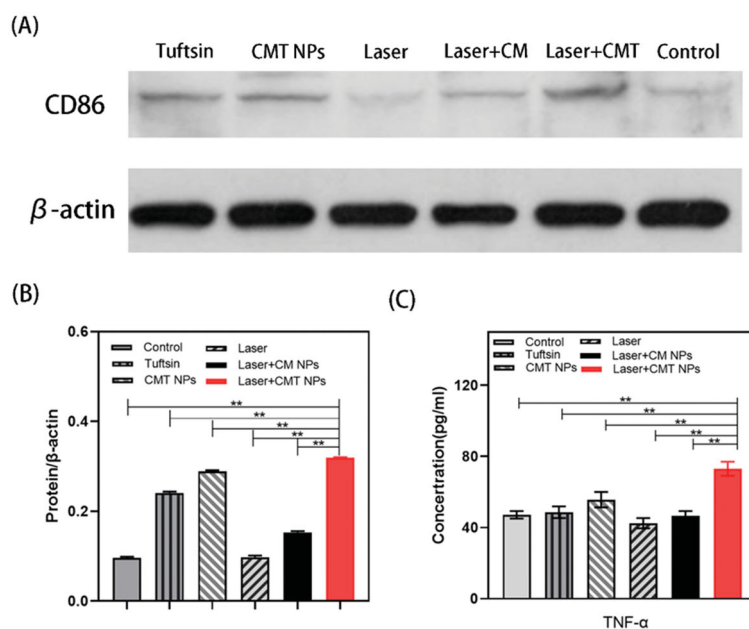

Figure 11. (A, B) The contents of CD86 in Y79 tumors after different treatments. (C) TNF-α levels in Y79 tumors after different treatments (**$p<.01$).

detected. As shown in the figure, the changes in routine blood parameters after CMT NPs injection were negligible compared with those in the control group. Finally, a biochemical blood test was performed. In the figure, the differences found in all groups were negligible, indicating that CMT NPs did not damage liver and kidney functions. All results indicated that no toxicity was detected in mice during the study period, indicating that CMT has a strong
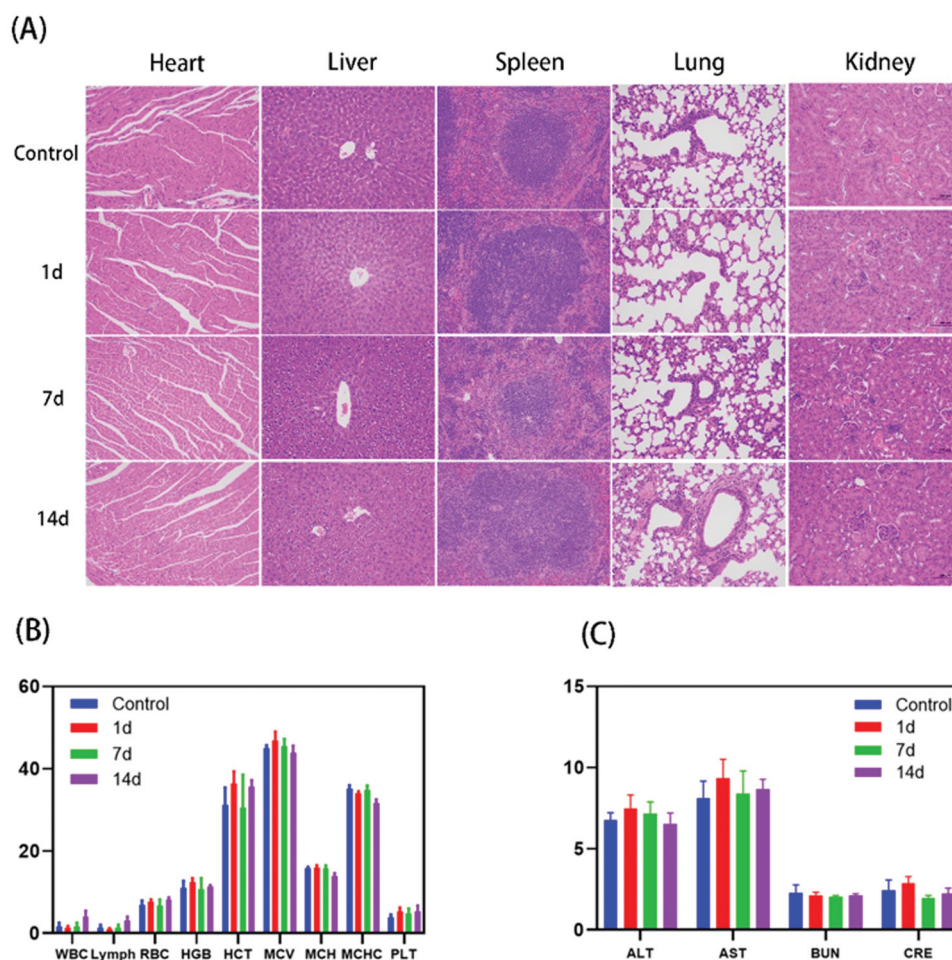
Figure 12. (A) H&E staining of main organs (heart, liver, spleen, lung, and kidney) of mice at day 1, 7, and 14 after CMT NPs injection. (B, C) Blood biochemistry and complete blood analysis of mice sacrificed at different time intervals (control, 1 days, 7 days, and 14 days) after intravenous injection of CMT NPs.

therapeutic effect with good biosafety in tumor treatment (Figure 12).

4. Conclusions

In conclusion, we developed the first multifunctional magnetic carbon CMT NPs for dual-mode imaging-guided laser/immunotherapy of Rb. The carbonized CM and CMT nanoparticles exhibited stable magnetic properties and carbon material characteristics, enabling the nanoparticles to simultaneously achieve PA/MR imaging. In addition, CMT NPs can achieve photothermal treatment due to its good photothermal transformation ability, leading to direct tumor apoptosis/necrosis, while tuftsin induces macrophages to differentiate into the M1 type, resulting in the secretion various antitumor cytokines, such as TNF-α. Synergistic treatment had a significant inhibitory effect on tumors without obvious recurrence. In addition, the nanoparticles showed high biocompatibility and biosafety *in vitro* and *in vivo*, which accelerated their clinical transformation. Therefore, our study provides compelling evidence that these nanoparticles constitute a potential nanoplatform to promote the effectiveness and high biosafety of cancer treatments.

References

An Y, Li L, Yang D, et al. (2014). Anticancer activity of tuftsin-derived T peptide in postoperative residual tumors. Anticancer Drugs 25: 1785–67.

Arranja AG, Pathak V, Lammers T, Shi Y. (2017). Tumor-targeted nanomedicines for cancer theranostics. Pharmacol Res 115:87–95.

Bowser BH, Brower LJ, Ohnsorg ML, et al. (2018). Comparison of surface-bound and free-standing variations of HKUST-1 MOFs: effect of activation and ammonia exposure on morphology, crystallinity, and composition. Nanomaterials 8:650.

Chanmee T, Ontong P, Konno K, Itano N. (2014). Tumor-associated macrophages as major players in the tumor microenvironment. Cancers 6:1670–90.

Chen H, Sulejmanovic D, Moore T, et al. (2014). Iron-loaded magnetic nanocapsules for pH-triggered drug release and MRI imaging. Chem Mater 26:2105–12.

Chen Q, Hu Q, Dukhovlinova E, et al. (2019). Photothermal therapy promotes tumor infiltration and antitumor activity of CAR T cells. Adv Mater 31:e1900192.

Chen Q, Xu L, Liang C, et al. (2016). Photothermal therapy with immune-adjuvant nanoparticles together with checkpoint blockade for effective cancer immunotherapy. Nat Commun 7:13193.

Cheng HW, Tsao HY, Chiang CS, Chen SY. (2021). Advances in magnetic nanoparticle-mediated cancer immune-theranostics. Adv Healthc Mater 10:e2001451.

de Maar JS, Sofias AM, Porta Siegel T, et al. (2020). Spatial heterogeneity of nanomedicine investigated by multiscale imaging of the drug, the nanoparticle and the tumour environment. Theranostics 10:1884–909.

Donahue ND, Acar H, Wilhelm S. (2019). Concepts of nanoparticle cellular uptake, intracellular trafficking, and kinetics in nanomedicine. Adv Drug Deliv Rev 143:68–96.

Fabian ID, Onadim Z, Karaa E, et al. (2018). The management of retinoblastoma. Oncogene 37:1551–60.

Fridkin M, Najjar VA. (1989). Tuftsin: its chemistry, biology, and clinical potential. Crit Rev Biochem Mol Biol 24:1–40.

Gerspach J, Pfizenmaier K, Wajant H. (2009). Improving TNF as a cancer therapeutic: tailor-made TNF fusion proteins with conserved antitumor activity and reduced systemic side effects. Biofactors 35:364–72.

Guerra AD, Yeung OWH, Qi X, et al. (2017). The anti-tumor effects of M1 macrophage-loaded poly (ethylene glycol) and gelatin-based hydrogels on hepatocellular carcinoma. Theranostics 7:3732–44.

Guo Y, Ran Y, Wang Z, et al. (2019). Magnetic-responsive and targeted cancer nanotheranostics by PA/MR bimodal imaging-guided photothermally triggered immunotherapy. Biomaterials 219:119370.

Haimov-Talmoud E, Harel Y, Schori H, et al. (2019). Magnetic targeting of mTHPC to improve the selectivity and efficiency of photodynamic therapy. ACS Appl Mater Interfaces 11:45368–80.

Hou X, Tao Y, Pang Y, et al. (2018). Nanoparticle-based photothermal and photodynamic immunotherapy for tumor treatment. Int J Cancer 143:3050–60.

Huo SH, An HY, Yu J, et al. (2017). Pyrolytic in situ magnetization of metal-organic framework MIL-100 for magnetic solid-phase extraction. J Chromatogr A 1517:18–25.

Jian J, Liu C, Gong Y, et al. (2014). India ink incorporated multifunctional phase-transition nanodroplets for photoacoustic/ultrasound dual-modality imaging and photoacoustic effect based tumor therapy. Theranostics 4:1026–38.

Kaewkhaw R, Rojanaporn D. (2020). Retinoblastoma: etiology, modeling, and treatment. Cancers 12:2304.

Karami A, Mohamed O, Ahmed A, et al. (2021). Recent advances in metal-organic frameworks as anticancer drug delivery systems: a review. Anticancer Agents Med Chem 21:2487–504.

Komohara Y, Fujiwara Y, Ohnishi K, Takeya M. (2016). Tumor-associated macrophages: potential therapeutic targets for anti-cancer therapy. Adv Drug Deliv Rev 99:180–5.

Lee C, Kwon W, Beack S, et al. (2016). Biodegradable nitrogen-doped carbon nanodots for non-invasive photoacoustic imaging and photothermal therapy. Theranostics 6:2196–208.

Li K, Zhang Y, Lin YZ, et al. (2019). Versatile functional porous cobalt-nickel phosphide-carbon cocatalyst derived from a metal-organic framework for boosting the photocatalytic activity of graphitic carbon nitride. ACS Appl Mater Interfaces 11:28918–27.

Li W, Yang J, Luo L, et al. (2019). Targeting photodynamic and photothermal therapy to the endoplasmic reticulum enhances immunogenic cancer cell death. Nat Commun 10:3349.

Liang Z, Qu C, Xia D, et al. (2018). Atomically dispersed metal sites in MOF-based materials for electrocatalytic and photocatalytic energy conversion. Angew Chem Int Ed Engl 57:9604–33.

Liu Y, Kangas J, Wang Y, et al. (2020). Correction: Photothermal conversion of gold nanoparticles for uniform pulsed laser warming of vitrified biomaterials. Nanoscale 12:20543.

Lu H, Wu L, Liu L, et al. (2018). Quercetin ameliorates kidney injury and fibrosis by modulating M1/M2 macrophage polarization. Biochem Pharmacol 154:203–12.

Mantovani A, Sica A, Locati M. (2007). New vistas on macrophage differentiation and activation. Eur J Immunol 37:14–6.

Munier FL, Beck-Popovic M, Chantada GL, et al. (2020). Conservative management of retinoblastoma: challenging orthodoxy without compromising the state of metastatic grace. "Alive, with good vision and no comorbidity". Prog Retin Eye Res 78:100857.

Musetti S, Huang L. (2018). Nanoparticle-mediated remodeling of the tumor microenvironment to enhance immunotherapy. ACS Nano 12:11740–55.

Nichols JW, Bae YH. (2014). EPR: evidence and fallacy. J Control Release 190:451–64.

Overchuk M, Zheng G. (2018). Overcoming obstacles in the tumor microenvironment: recent advancements in nanoparticle delivery for cancer theranostics. Biomaterials 156:217–37.

Piña Y, Boutrid H, Murray TG, et al. (2010). Impact of tumor-associated macrophages in LH(BETA)T(AG) mice on retinal tumor progression: relation to macrophage subtype. Invest Ophthalmol Vis Sci 51:2671–7.

Qiu X, Zhao T, Luo R, et al. (2022). Tumor-associated macrophages: key players in triple-negative breast cancer. Front Oncol 12:772615.

Riley RS, June CH, Langer R, Mitchell MJ. (2019). Delivery technologies for cancer immunotherapy. Nat Rev Drug Discov 18:175–96.

Singh N, Qutub S, Khashab NM. (2021). Biocompatibility and biodegradability of metal organic frameworks for biomedical applications. J Mater Chem B 9:5925–34.

Song G, Kenney M, Chen YS, et al. (2020). Carbon-coated FeCo nanoparticles as sensitive magnetic-particle-imaging tracers with photothermal and magnetothermal properties. Nat Biomed Eng 4:325–34.

Väyrynen JP, Haruki K, Lau MC, et al. (2021). The prognostic role of macrophage polarization in the colorectal cancer microenvironment. Cancer Immunol Res 9:8–19.

Wang HF, Ran R, Liu Y, et al. (2018). Tumor-vasculature-on-a-chip for investigating nanoparticle extravasation and tumor accumulation. ACS Nano 12:11600–9.

Wang M, Yang Q, Li M, et al. (2020). Multifunctional nanoparticles for multimodal imaging-guided low-intensity focused ultrasound/immunosynergistic retinoblastoma therapy. ACS Appl Mater Interfaces 12:5642–57.

Wu M, Xiong H, Zou H, et al. (2018). A laser-activated multifunctional targeted nanoagent for imaging and gene therapy in a mouse xenograft model with retinoblastoma Y79 cells. Acta Biomater 70:211–26.

Wu MX, Yang YW. (2017). Metal-organic framework (MOF)-based drug/cargo delivery and cancer therapy. Adv Mater 29.

Xia W, Qiu B, Xia D, Zou R. (2013). Facile preparation of hierarchically porous carbons from metal-organic gels and their application in energy storage. Sci Rep 3:1935.

Yamamoto N, Sery TW, Hoober JK, et al. (1994). Effectiveness of photofrin II in activation of macrophages and in vitro killing of retinoblastoma cells. Photochem Photobiol 60:160–4.

Zhang S, Lu Q, Wang F, et al. (2021). Gold-platinum nanodots with high-peroxidase-like activity and photothermal conversion efficiency for antibacterial therapy. ACS Appl Mater Interfaces 13:37535–44.

Zhi D, Yang T, O'Hagan J, et al. (2020). Photothermal therapy. J Control Release 325:52–71.